Symmetry constrained neural networks for detection and localization of damage in metal plates

James Amarel,[1, a)] Christopher Rudolf,[2, b)] Athanasios Iliopoulos,[3] John Michopoulos,[4] and Leslie N. Smith[5]

[1)]*NRC Research Associate, U.S. Naval Research Laboratory, Washington, DC, 20375, USA*

[2)]*Multifunctional Materials Branch, U.S. Naval Research Laboratory, Washington, DC, 20375, USA*

[3)]*Center for Materials Physics and Technology, U.S. Naval Research Laboratory, Washington, DC, 20375, USA*

[4)]*Principal Scientist of Materials Innovation, U.S. Naval Research Laboratory, Washington, DC, 20375, USA*

[5)]*Navy Center for Applied Research in Artificial Intelligence, U.S. Naval Research Laboratory, Washington, DC, 20375, USA*

(Dated: 30 September 2024)

The present paper is concerned with deep learning techniques applied to detection and localization of damage in a thin aluminum plate. We used data collected on a tabletop apparatus by mounting to the plate four piezoelectric transducers, each of which took turn to generate a Lamb wave that then traversed the region of interest before being received by the remaining three sensors. On training a neural network to analyze time-series data of the material response, which displayed damage-reflective features whenever the plate guided waves interacted with a contact load, we achieved a model that detected with greater than 99% accuracy in addition to a model that localized with 2.58 ± 0.12 mm mean distance error. For each task, the best-performing model was designed according to the inductive bias that our transducers were both similar and arranged in a square pattern on a nearly uniform plate.

I. INTRODUCTION

Structural health monitoring (SHM) plays a crucial role in enhancing the reliability, safety, and lifespan of critical structures and equipment, including automatic drivelines[1], bridges[2], concrete buildings[3], and airplane wings[4,5]. Integrating sensors directly into system components facilitates real-time monitoring, which allows for the early detection of potential issues, such as cracks, corrosion, material loss, and delamination[6], thereby extending service lifetimes. Furthermore, minor problems can be prevented from escalating into catastrophic failures by following maintenance strategies prescribed according to the better-informed risk profiles made available by intelligent sensing.

Nondestructive evaluation techniques are of particular interest for material integrity determination. In this respect, Lamb waves are especially desirable, for they are able to travel long distances with low attenuation. Furthermore, there exist standard procedures for their generation through the use of specimen mounted piezoelectric transducers[7–10]. Moreover, Lamb waves feature multiple vibrational modes, each of which offers varying sensitivity to different types of defects[11].

Through acoustic wave interrogation methods, previous workers have advanced solutions via a number of signal-processing techniques, physical considerations, and neural network designs. The integration of deep learning techniques into SHM routines has been shown to elevate the capabilities of predictive maintenance algorithms[12–16]. These approaches excel relative to those based on classical computing algorithms in the complex noisy environments common to real-world use cases.

A hybrid data-driven/mechanistic approach for characterizing material defects is that of physics-informed neural networks[17]. Also through the use of known physics, Zhang et al.[18] leveraged calculated time-of-flight deviations together with a convolutional neural network (CNN) to reconstruct an image indicating the probability of damage in each of the possible defect locations. For complex systems, however, it is less clear how to employ approximate governing equations to deduce the location and nature of damage from modifications to the response caused by wave-defect interactions. Indeed, effects due to specimen boundaries, manufacturing processes, and sensor bonding are challenging to capture analytically[19–23]. Furthermore, understanding the dispersive nature of Lamb waves, their temperature dependence, and the nonlinear material response also demands significant time investment from subject-matter experts if either physics models or manual feature-extraction techniques are to be utilized[24]. Of the possible features to extract, a set that includes arrival times, amplitudes, spectral coefficients, and time-correlation functions, it remains unclear how to form the optimal descriptor. Alternatively, one can train deep learning algorithms to implicitly extract the relevant damage indices directly from data[25,26].

Rai et al.[27] feed raw time-domain signals into a 1D CNN for detection of notch-like damage. Xu et al.[28] located fatigue cracks with a 1D-attention-CNN, using

---
[a)]Electronic mail: james.l.amarel4.ctr@us.navy.mil
[b)]Electronic mail: christopher.c.rudolf.civ@us.navy.mil
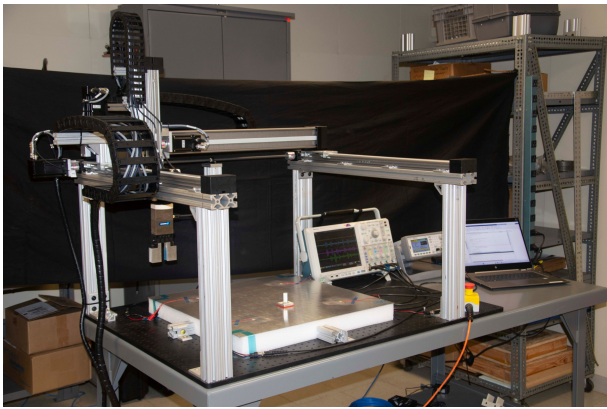
FIG. 1: Photo of the experimental apparatus showing the gantry, the aluminum plate, the piezoelectric transducers, and the contact load in addition to the waveform generating oscilloscope and a laptop that runs the code responsible for controlling the gantry.

wavelet coefficients as features. From time-frequency representations, one can both detect anomalies[29,30] and localize cracks[31] using image-based techniques. Mariani et al.[32] found that using an adaptation of the causal convolutional WaveNet architecture while forgoing conventional baseline-subtraction methods afforded robust generalization capabilities when detecting defects in the presence of data distribution shift due to operating temperature variations. Palanisamy et al.[33] investigated how to transfer knowledge from a neural network trained on sparse sensor network data from one component to another. It is an ongoing challenge to successfully transition laboratory developed algorithms to their intended real-world use cases[34]. Song et al.[35] utilized neural network layers with both global and local context to localize damage in carbon fiber-reinforced plastic laminate. They used spherical damping soil placed within a square region between four piezoelectric transducers as a proxy for damage. Use of a square array of transducers is common practice in the literature[36,37].

In our experiment (see Figure 1), one transducer is placed near each corner of a square plate and a contact load of square geometry is used as a damage proxy. This sensor grid formally admits a geometric inductive bias, which yields as constraints a set of necessary conditions on the neural network architecture that in idealized conditions can be expected to increase per parameter expressivity and bolster model generalizability[38]; while one cannot fully specify the architecture by such reasoning, it does follow from these principled symmetry arguments that the multi-sensor data should be fused by viewing the measured signals as living on a four-node graph. In this way, the transducers live on nodes while the edges represent messages carried by Lamb waves[39].

Real systems typically lack perfect symmetry, and the nature of the symmetry breaking is often incompletely characterized. Consequently, it is not clear to what ex-

tent one should hamper the flexibility of an ordinary neural network by baking into the architecture a notion of equivariance. Ideally, one could retain the flexibility of ordinary neural networks while also realizing the improvements to both robustness and generalizability that follow from symmetry constrained modeling.

Even in the presence of exact symmetry, the problem of determining the optimal network architecture remains unsolved. The situation is further complicated by the problem specific nuances of symmetry breaking. That our results show a favorable outcome on using a slightly modified form of the approximately equivariant structure proposed by Wang et al.[40] calls for further investigation into symmetry as an ingredient in next-generation SHM routines. Such research, together with interpretations of the learned symmetry-breaking, could provide insights into the physical system, refine confidence estimates of model predictions, and facilitate the development of techniques for achieving more consistent performance when transferring trained models to different structures or equipment.

In the following, we present the first study on the effects of incorporating equivariance, both exact[38] and approximate[40], associated with sensor-network geometry into a deep learning algorithm tasked with detecting and localizing damage from data reflecting acoustic wave propagation in thin plates. In doing so, we exhibit the benefits of symmetry-aware modeling and systematically address difficulties reported by previous authors[11,41] when measurements corresponding to different damage states are related by symmetry transformations.

This paper is organized as follows. In section II, we describe and visualize the data. Then, for the reader's convenience, we discuss our results in section III before considering the technical definitions of our neural network architectures, which are given in section IV. Finally, in section V we state our conclusion.

Our code makes use of the deep learning library Lux.jl[42] and the plotting software CairoMakie.jl[43].

II. DATA

Attached to an aluminum 6061-T6 plate of side length 610 mm and thickness 1.2 mm are four APC International Model 63 piezoelectric transducers arranged in a square grid of length 350 mm on its sides. A single 300 kHz, 5 count, Hanning-windowed tone burst generates a vibrational waveform in one corner of the plate that then travels through the bulk, thereby interacting with material inhomogeneities, before ultimately being registered by three passive sensors in the flight path (see Figure 2). For each contact load configuration, we then repeat this procedure to collect response measurements resulting from the generation of a propagating wave in each corner. As a result, we associate with every damage state a collection of sixteen time-series signals, each
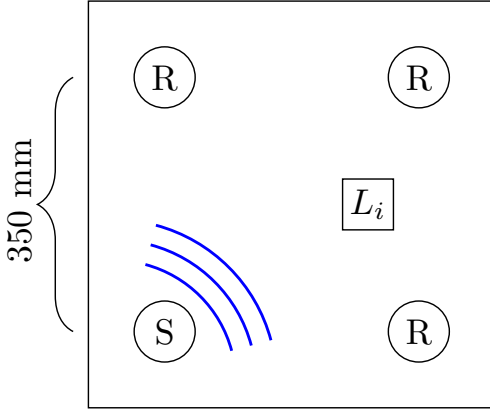
FIG. 2: Plate schematic for Lamb wave source S in the presence of a contact load at position L_i that redirects waves into receivers R.
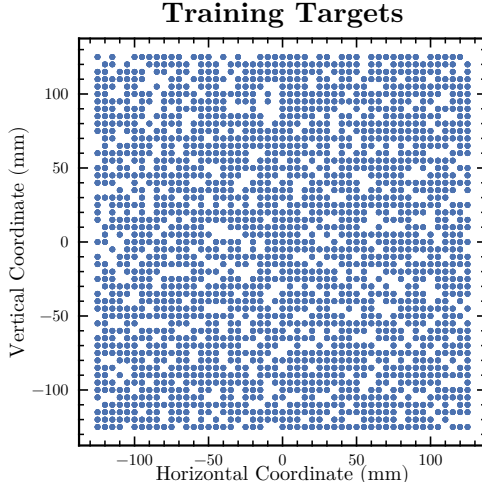

Training Targets

FIG. 3: A typical uniform initialization of a training set covering 80% of the possible load locations.

of which contains $10,000$ piezoelectric voltage measurements sampled at equal intervals over a time window of 0.4 ms following signal transmittance.

In total, the dataset used in this paper comprises 2601 damaged examples, each of which corresponds to the contact load being placed in a different location within the square of area $0.275m^2$ concentric to the region bounded by our transducers, in addition to 6 baseline examples where the contact load is absent. Half of the baseline examples were determined at the beginning of data collection while the remaining three were measured after all of the damaged examples had been acquired. The contact load face, which is of a square geometry with 40 mm side length, couples to the plate via a 0.125 inch thick silicone sheet of 10A durometer. A $51x51$ square lattice (see Figure 3) is generated by placing the contact load at 5 mm intervals.
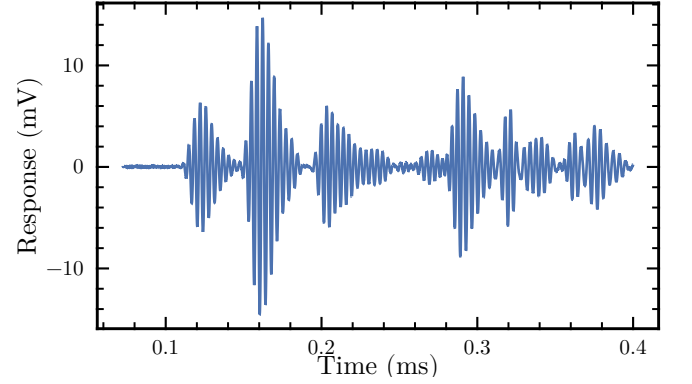
Those locations in Figure 3 without a marker are either in the test set or one of the examples that we discarded.

Baseline Signal (Edge)
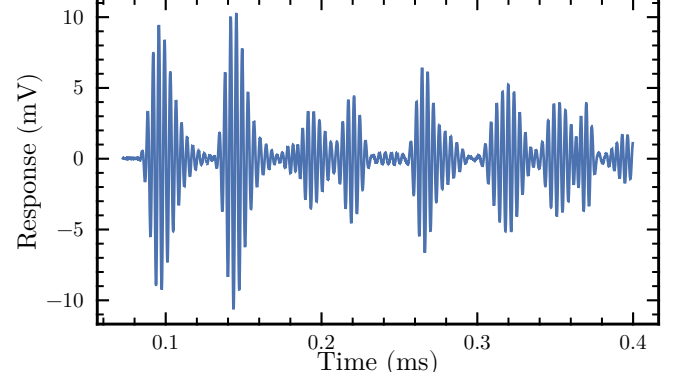
(a) Baseline signal received across the edge path.

Baseline Signal (Diagonal)

(b) Baseline signal received across the diagonal path.

FIG. 4: Average full-fidelity received baseline signals.

We rejected as poor quality 12 examples containing generated signals with spectral densities far from their intended form. Additionally, we removed from our dataset 8 examples containing received signals that were uncharacteristically far, as measured by Euclidean distance, to the appropriate mean received signal. When using the baseline-subtraction technique, we also discarded 12 examples that developed atypically large maximum signal amplitudes.

A. Compressed Signals

The raw received signals resolve details of wave propagation at fidelities unnecessary for both localization and detection (see Figure 4). Compression of the signals can be achieved by examining their spectra. The dominant Fourier modes are contained within the $180kHz - 420kHz$ interval[44] (see Figure S3). Our implementation of such a high and low pass filter yielded, after back-transforming to real space, a time-series signal reduced from $10,000$ to 192 elements in length. Then, discard-

ing times before the signal had a chance to reach the receivers, trimmed to length 158 the time sequences.

Having effectively reduced the sampling rate and filtered out high frequency noise, the difference between baseline and damaged signals is readily visualized (see Figure 5). Indeed, contact load induced attention is apparent in the $0.20 - 0.24$ ms time window where the lowest-order antisymmetric longitudinal mode A_0 is expected to arrive when traveling across the plate diagonal. Of second most importance for localization are the A_0 waves that were reflected into a receiver by the specimen boundary; for diagonal wavepaths, we recorded these signals in the time window $0.32 - 0.37$ ms. Though subdominant relative to the above two contributions, the symmetric modes (both longitudinal and shear) that arrive before A_0 (see Figure 4) also carry information pertaining to the material damage state.

B. Structure of input data

To each damaged state, i.e., contact load center of mass vector $\mathbf{x}$, we associated an adjacency matrix of sixteen time-series signals $V_{rs}(t)$ of length 158, one for each configuration specified by r, s, the receiver and the sender index, respectively (see Figure 6). This way, the measured signals could be viewed as living on a four-node graph, with transducers as the nodes and the edges corresponding to messages carried by Lamb waves[39]. When the dihedral group is an exact symmetry, this graph forms a homogeneous space that demands an equivariant architecture.

III. RESULTS

Loss and accuracy evolution curves, in addition to cumulative error distributions were obtained from results for model performance across 6 different training initializations, i.e., model parameters and train/test split. We investigate three model types: 1) an *ordinary* convolutional neural network, 2) an *exactly equivariant* neural network, and 3) an *approximately equivariant* neural network. These models were designed similarly in all respects except for their treatment of the square group symmetry. Both symmetry-aware models possessed about $366,000$ trainable parameters, while the *ordinary* model operated with about $371,000$ trainable parameters.

For training, we used the Adam optimizer[45] with batch size 32 and the OneCycle[46] learning schedule defined by an initial learning rate of 10^{-5} that ramps for 200 epochs until reaching strength 2.5×10^{-3} before descending over the final 800 training epochs. We used final learning rates of 10^{-3} and 10^{-7} for the training of our locators and our detectors, respectively.

Only the *exactly equivariant* model offered predictions constrained to transform under changes of coordinates

	Exact (mm)	Approx. (mm)	Ordinary (mm)
MDE	2.93 ± 0.11	2.58 ± 0.12	2.98 ± 0.14
Var.	1.84 ± 0.12	1.61 ± 0.11	1.92 ± 0.18
RMSE	1.46 ± 0.09	1.24 ± 0.08	1.55 ± 0.17
Gap	1.07 ± 0.10	0.84 ± 0.09	0.99 ± 0.18

TABLE I: Test performance, as measured by the mean distance error (MDE), the variance of the distance errors (Var.), the root mean square error (RMSE), and the generalization gap (Gap).

generated by symmetry operations like vectors, in the case of localization, or scalars, in the case of detection; however, the *approximately equivariant* model is initialized in an equivariant state and possessed limited degrees of freedom for violating square symmetry (see section IV B).

A. Localization

Toward optimizing model parameters, we first constructed the train/test datasets by uniformly sampling locations to be held out at a $80\%/20\%$ ratio. Then, as a form of data augmentation, we used baseline-subtraction to associate with each target location six signals. For the training dataset, each baseline-subtracted example was treated individually with respect to mini-batching. However, each test prediction was the result of averaging the model output over all six baseline-subtracted inputs. This asymmetric treatment is expected to equip the trained model with a statistical advantage against drift in operating conditions during data acquisition[47].

Each model is trained (see Figure 7) using the following the pairwise loss

$$\mathrm{E}(\hat{\mathbf{x}}, \mathbf{x}) = |\hat{\mathbf{x}} - \mathbf{x}|^2 \big[1 - A(\hat{\mathbf{x}}, \mathbf{x})\big] \theta(|\hat{\mathbf{x}} - \mathbf{x}|, 0.5\lambda_{A_0}), \quad (3.1)$$

where $\hat{\mathbf{x}}$ and $\mathbf{x}$ point to the center of mass of the ground-truth contact load and the predicted contact load, respectively, A gives the percentage area overlap between the predicted and ground-truth contact load faces, and θ is the Heaviside function with arguments to ensure that no loss is accumulated for predictions with distance errors less than the diffraction limit, i.e., one-half of the A_0 mode wavelength, $\lambda_{A_0} = 6.70$ mm.

Out of the three models we studied, the *approximately equivariant* model attained the lowest mean values on all four metrics listed in Table I. Evidently, the weak constraints imposed upon the *approximately equivariant* model typically facilitated decreased variance and reduced generalization gap relative to both the strictly constrained and unconstrained architectures. By allowing for weak symmetry breaking, we achieved a better model with respect to metrics sensitive to both gross performance (MDE) and worst case predictions (RMSE).
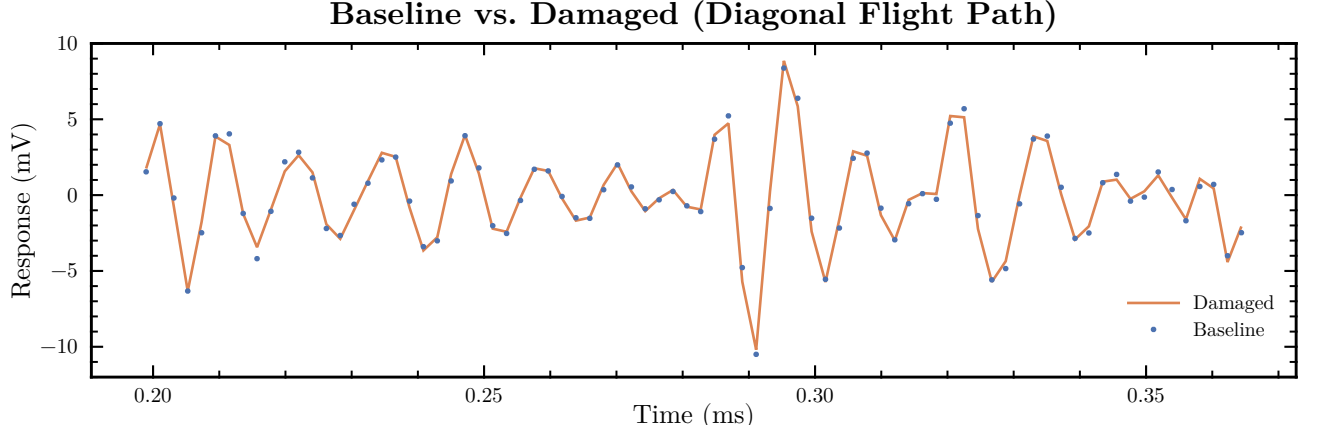
FIG. 5: Comparison of a baseline signal that propagated along a plate diagonal in the absence of a contact load with a signal corresponding to a damaged state that followed the same flight path. Both signals have been compressed from their raw form by way a high and a low pass filter.
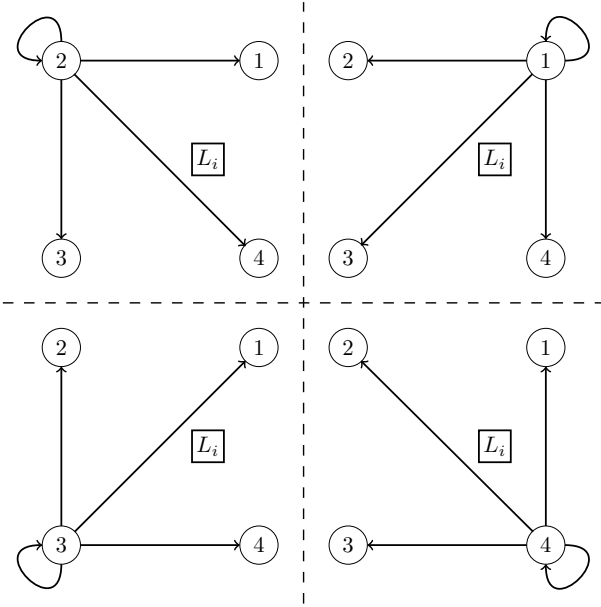

FIG. 6: Visual representation of the adjacency matrix structure, for an example with load location L_i. Diagonal elements correspond to self interactions, while off-diagonal terms correspond to messages carried by Lamb waves across the plate for a given receiver-sender pair.

Predictions by all three models studied herein were correct within 13.4 mm for 99.9% of test data. The *approximately equivariant* model typically offered predictions within the diffraction limit on more than 70% of the test examples (see Figure 9). Only the *ordinary* model admitted test predictions of error greater than 16.75 mm.

Generically, the difficult examples are those corresponding to load locations on the edges of the square region sampled by our dataset (see Figure S5 in Supple-
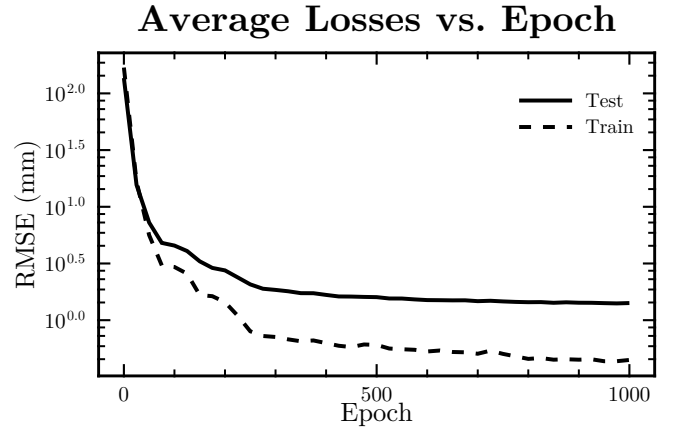

FIG. 7: Test and train optimization loss evolution averaged across all initializations and models. RMSE is the root mean square error.
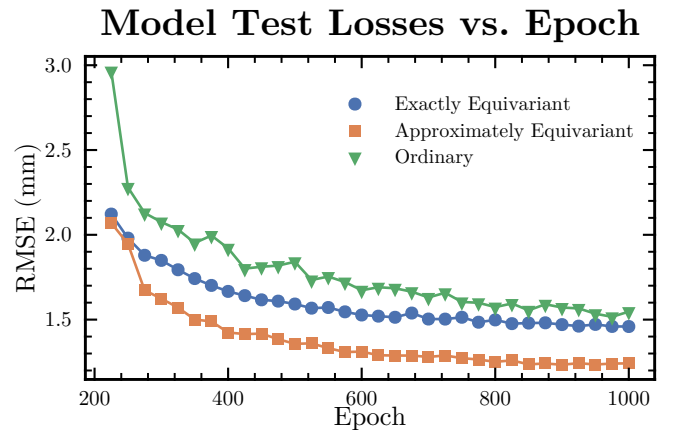

FIG. 8: Comparison across models of the root mean square error (RMSE) evolution averaged across all initializations.
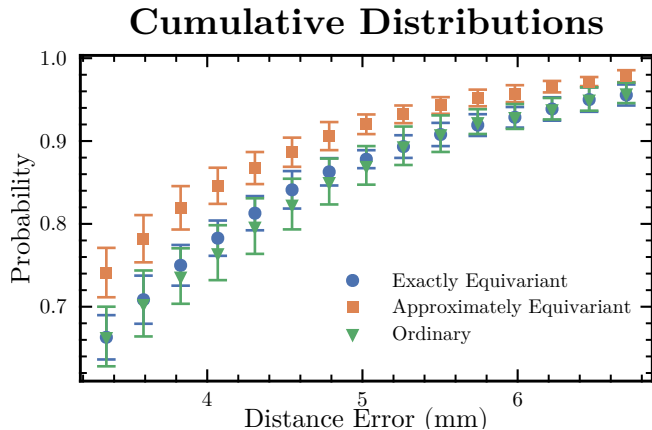
Cumulative Distributions

FIG. 9: Comparison of truncated, initialization averaged, cumulative distributions on test data. All three models studied herein typically capture greater than 95% of test data with errors less than 6.70 mm.

Time Window (ms)	Mean Distance Error (mm)
0.07 - 0.40	2.81 ± 0.12
0.16 - 0.40	3.05 ± 0.21
0.07 - 0.24	7.41 ± 0.43
0.16 - 0.24	10.39 ± 0.71

TABLE II: Comparison of mean model performance when ingesting the full compressed signal (0.07 - 0.40 ms), vs. discarding the early to arrive symmetric mode (0.16 - 0.40 ms), vs. truncating wave reflections (0.07 - 0.24 ms), vs. windowing only the directly received A_0 mode (0.16 - 0.24 ms).

mentary Information II). Boundary regions present substantial challenges in structural health monitoring due to sparse sampling and the breakdown of translation equivariance. For damage locations near the boundary of our sample grid, both the *exactly equivariant* and the *approximately equivariant* architectures outperformed the *ordinary* model, yielding lower mean errors and reduced uncertainty (see Figure S5 and Figure S6 in Supplementary Information II). This improvement is attributed to the weight sharing mechanism inheret to group convolutions, which facilitates the learning of features that generalize across symmetry related examples.

On evaluating the vector distance between transformed model predictions and model predictions for transformed inputs, we found that the *approximately equivariant* model and the *ordinary* model learned to violate equivariance on the boundary by 80 mm and 180 mm, respectively (see Figure S7 in Supplementary Information II). While some metrics (see Figure S1, Figure S2, Figure S4, and Figure S3 in Supplementary Information I) suggest that square symmetry is not weakly broken in our system, inspection of the symmetry-breaking weights reveals that the approximately equivariant model learned latent feature maps that exhibited diminishing equivariance violations with increasing layer depth (see Figure S8 in Supplementary Information II). In the final layer, the symmetry-breaking weights deviated by less than 6% from their symmetry-preserving form.

1. Time-Window Ablation

The input data exhibits features reflecting the multimode composition of the plate's vibrational spectrum together with interactions between directly received waves and those that are redirected by the plate boundaries. Although one might anticipate beneficial effects would follow from selectively windowing the directly received lowest-order antisymmetric longitudinal mode A_0, as these excitations tend to leak most strongly into contact loads, we empirically concluded that this act of manual feature selection is detrimental to model performance. Models that ingested the entire signal after data curation consistently performed better than those that either windowed the A_0 mode, truncated signal regions containing reflections, or discarded the early to arrive symmetric modes (see Table II). Evidently, neural network based structural health monitoring solutions do not require extensive physical modeling in order to glean useful information from measurements of multi-mode acoustic excitations that underwent scattering events before arriving at a transducer[11].

B. Detection

In order to train a detector, we first addressed the class imbalance of our dataset by forming synthetic normalized linear combinations of the six raw baseline examples until the damaged and undamaged pairs were equal in number[48]. Binary cross-entropy served as our optimization loss (see Figure 10).

For all three models studied herein, we achieved over 99% mean accuracy on averaging across the different initializations when using a 20%/80% ratio for our train/test split. Final average training accuracies were 0.998 ± 0.001, 0.998 ± 0.001, and 0.998 ± 0.002, for the *exactly equivariant*, *approximately equivariant*, and *ordinary* models, respectively (see Figure 11). Throughout this subsection, error bars are computed as the difference between the mean value of a quantity and its observed value nearest unity. With perplexity defined here as the natural exponential of the cross-entropy, we observed final perplexity values of 1.009 ± 0.004, 1.008 ± 0.004, and 1.009 ± 0.006 for the *exactly equivariant*, *approximately equivariant*, and *ordinary* architectures, respectively.

Though all three models converged to states offering similar performance, the symmetry-aware models required fewer training epochs than the *ordinary* model. This may be because attenuation is recognizable (see Fig-
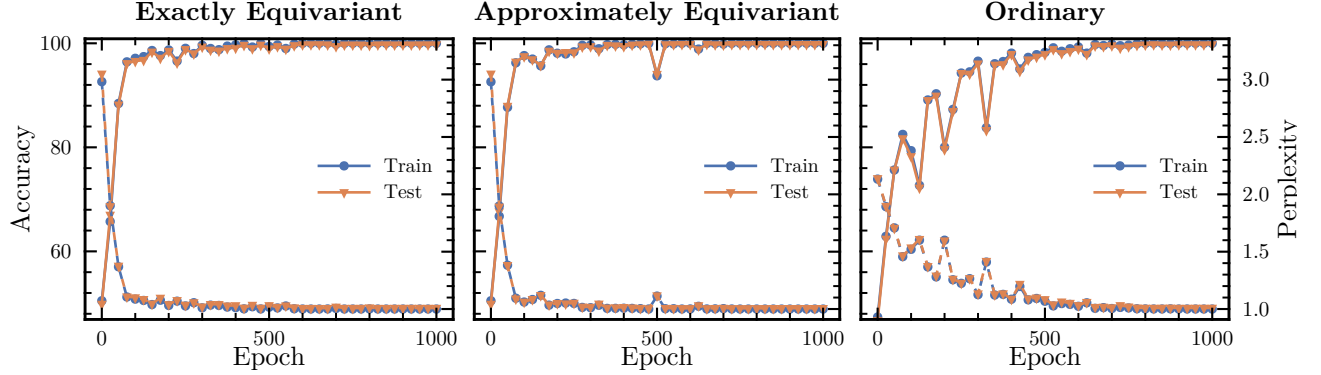
Detector Training Convergence

FIG. 10: Accuracy and loss vs. epoch curves averaged over initializations for each architecture.

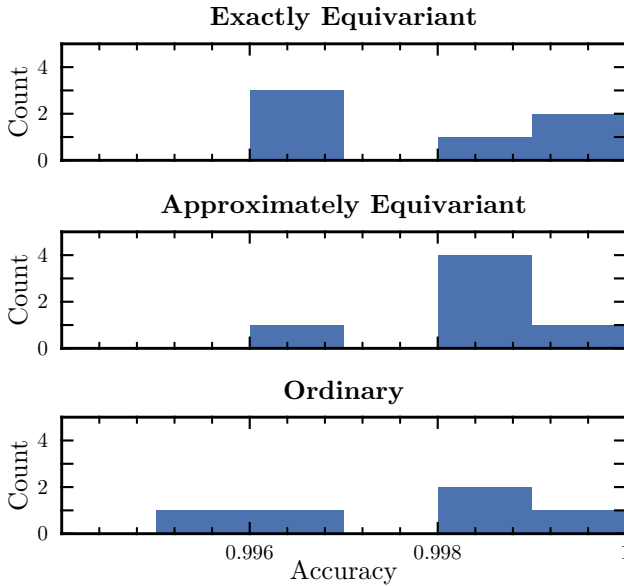## Accuracy Histograms over Initializations

FIG. 11: Histograms of final detector accuracies over distinct training initializations.

ure 5) with less regard for those spatial inhomogeneities affecting arrival times that must be learned by the localizer models.

IV. MODELS

We studied three neural networks trained to recognize signatures of the interactions between vibrational waves propagating through a thin-plate specimen and a contact load, which is to be either detected or located, that tends to absorb incoming wave energy and thereby serves as a proxy for corrosion damage. This task can be viewed as an inverse problem in which one seeks to infer the state of a material from response measurements.

To this end, we first trained a 6-block *ordinary* convolutional neural network in which the first five blocks contained a convolutional layer of kernel size equal to the input sequence length that was symmetrically padded such that the outgoing sequence length became half that of the input sequence length. The receiver and sender indices (see Figure 6) were treated as channels. Nonlinearities were omitted in the first block, which used a length 158 kernel. Internal layers included a skip connection followed by LayerNorm[49] and the *swish*[50] activation function. In order to reduce internal layer inputs to the same size as their output, as required by the skip connection, we convolved against a non-trainable averaging kernel with the same padding and size as the associated trainable convolution. For the last block, where boundary effects were present in the time-series, a dense layer acted on both channel and time indices. Then, activation by *tanh* preceded a final dense layer that yielded an output array with two components, which was taken to contain the horizontal and vertical coordinates of the load location. Our models were regularized by weight decay value of strength 10^{-6} and 0.05 probability of dropout on the channel index.

On considering symmetries as a guiding principle for model design, it follows that there are a number of constraints on the architecture that must be satisfied. These priors demand that the trainable weights be shared in a manner consistent with time-translation invariance, the arrow of time, and the square group[38]. In idealized conditions, this is expected to maximize the expressivity of each neuron, ultimately yielding a model that is better suited to perform on noisy data.

Time-translation invariance, modulo boundary effects, and the arrow of time are readily enforced by using layers with the standard convolutional action on the time index. The use of varying lead lengths for transducer-oscilloscope communication further motivated convolutional architectures, since invariance to time-shifts is desired. Because only affine layers admit

shift equivariance[51], the arbitrariness of our choosing a reference voltage is reflected only by omitting zero-frequency modes from the signal data. The scale invariance required by our freedom in choice of units can be satisfied by appropriately applying LayerNorm. Lastly, owing to the square arrangement of the piezoelectric sensors, it remains to incorporate equivariance with respect to symmetry transformations in the square group.

An *exactly equivariant* architecture assumes that the only significant spatial structure in our data is that of the sensor geometry and the load location; however, this idealization is not borne out by the data. Hence, we also put forth an *approximately equivariant* architecture that possesses a small fraction of symmetry-breaking weights for the purpose of capturing those aspects of both the plate and the transducers that produce deviations from system homogeneity even in the absence of damage (see Figure S2 in Supplementary Information I).

A. Dihedral group convolution

Here, we view the features $V_{sr} = V(e_s, e_r)$ as a bi-linear map defined by its action on the canonical basis vectors e, where $r, s \in \mathbb{Z}_4$ correspond to the receiver and sender transducer labels, respectively. On noting that r, s transform jointly under permutations $\sigma \in D_4$, with D_4 the square group, it follows that the linear action of the first, lifting, layer of the group convolutional neural network must take the form[38]

$$\tilde{V}_\sigma = \sum_{r,s \in \mathbb{Z}_4} K(\sigma^{-1} e_s, \sigma^{-1} e_r) V_{rs}, \qquad (4.1)$$

where σ is realized in its four-dimensional representation and K is the convolutional filter. Note that the time arguments of $V_{rs}(t)$ are suppressed in this section. Together with summing over the base space $\mathbb{Z}_4 \otimes \mathbb{Z}_4$ in Equation 4.1, we include a time convolution, for the relevant group to our system is that of time translations, cyclic rotations, and roto-reflections. With $\tilde{V}$ a function on D_4, we use the right regular representation for our internal layers, as this renders admissible pointwise nonlinearities[52]. The internal linear actions of the network can then be expressed

$$\hat{V}_\sigma = \sum_{\pi \in D_4} K(\sigma^{-1} \pi) \tilde{V}_\pi. \qquad (4.2)$$

To obtain a vector output $\mathbf{v}$ with components v^i from features $\hat{V}_\sigma$ in the regular representation, we contract the rotation matrices R_σ^{ij} along both the group index σ and a channel index j of dimension two according to

$$v^i = \sum_{\sigma \in D_4} \sum_{j \in \mathbb{Z}_2} R_\sigma^{ij} \hat{V}_\sigma^j. \qquad (4.3)$$

The above development is used in the construction of our *exactly equivariant* model (see Figure 12).
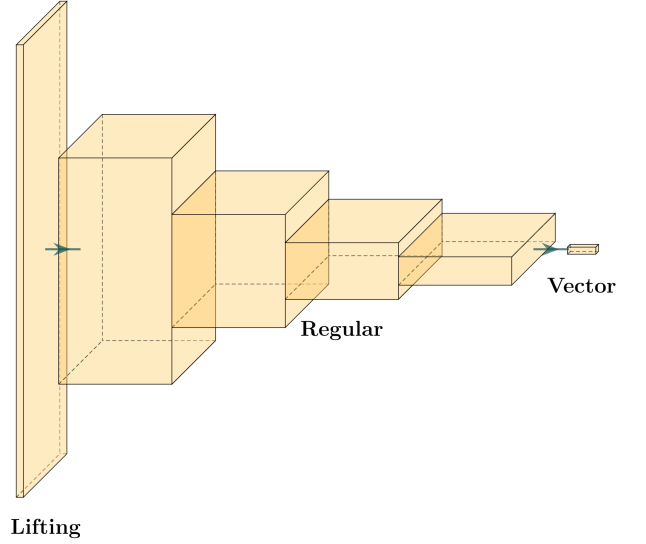

FIG. 12: Schematic of the model architecture[53]. Each of the lifting and regular blocks contain a convolutional layer. Height indicates time-sequence length, depth reflects the channel number, and width corresponds to the group index.

We note that an equation analogous to Equation 4.3 can be used to output a p4m-equivariant[38] grid suitable for probability imaging.

B. Approximately equivariant convolution

A complicating feature of our specimen is its inherent anisotropy caused by the rolling process used in manufacturing, which affects wave propagation and implies that the measured response is not independent of transducer location. Similarly, effects due to boundary irregularities and bulk material inhomogeneities violate square symmetry. Further symmetry-breaking effects stem from non-ideal aspects of Lamb wave generation.

If the symmetry-breaking is sufficiently weak, then incorporating a notion of approximate equivariance remains well motivated. This can be achieved in a manner that retains the structure of a strictly constrained neural network by introducing arrays containing eight symmetry-breaking trainable weights

$$\omega(g) = 8 \times \text{softmax}(g/8), \qquad (4.4)$$

and augmenting the group convolution[40]

$$\hat{V}_\sigma \to \omega(\sigma) \sum_{\pi \in D_4} K(\sigma^{-1} \pi) \tilde{V}_\pi. \qquad (4.5)$$

The weights in Equation 4.4 can be analogously introduced to Equation 4.1 and Equation 4.3. Note that Equation 4.4 is chosen to ensure that the elements of ω are positive definite, bounded from above, and do not introduce a superfluous trainable scale degree of freedom. It

is through Equation 4.5 that we constructed our *approximately equivariant* model.

V. CONCLUSION

We compared three neural network architectures on their ability to both detect and infer the location of contact loads placed on an aluminum plate from time-series measurements of the material response. Two of these architectures were designed to be aware of the geometry associated with our sensor network, while the third architecture was not equipped with equivariance as an inductive bias.

In the presence of symmetry breaking effects due to both material irregularities and imperfect sensor function, we designed an approximately equivariant neural network that achieved a mean distance error of 2.58 ± 0.12 mm. Tasked with the same problem, our ordinary and exactly equivariant models attained 2.98 ± 0.14 mm and 2.93 ± 0.11 mm mean distance error, respectively. The approximately equivariant model also reached the lowest optimization loss, which penalizes poor predictions more heavily than the mean distance error metric. By capturing 99% percent of test examples with errors less than 10.05 mm, all three of our models, together with our dataset, constitute state-of-the-art results with respect to localizing damage using machine learning techniques together with Lamb wave sensing.

When detecting the presence of a contact load on the plate, we attained over 99% accuracy with each of the three models studied herein. The symmetry aware models required fewer training epochs to reach this level of performance.

Our work demonstrates that equivariance constraints are beneficial in the complex and noisy scenarios that can be expected in real-world structural health monitoring applications. Future research may include using contact loads of varying geometry across multiple temperatures in addition to the localization and detection of crack-like damage.

ACKNOWLEDGMENTS

AUTHOR DECLARATIONS

Conflict of Interest

The authors have no conflicts of interest to disclose.

Author Contributions

JA: Conceptualization (lead), Data Curation (equal), Formal Analysis (lead), Methodology (lead), Software (lead), Validation (lead), Visualization (lead), Writing/Original Draft Preparation (lead), Writing - review and editing (equal). **CR**: Conceptualization (supporting), Data Curation (equal), Funding acquisition (lead), Investigation (supporting), Writing – review and editing (equal), Resources (equal). **AI**: Conceptualization (supporting), Data curation (equal), Methodology (supporting), Writing - review and editing (equal), Investigation (support), Resources (equal), Software (support), Validation (support). **JM**: Conceptualization (supporting), Methodology (supporting), Writing-review and editing (equal), Investigation (support), Resources (equal), Software (support), Validation (support). **LNS**: Conceptualization (supporting), Methodology (supporting), Writing - review and editing (equal), Resources (equal).

DATA AVAILABILITY

The code and compressed data needed to reproduce the findings of this study are openly available at `https://github.com/jameslamarel4/MINC/`. Raw data is available from either corresponding author upon reasonable request.

[1] B. Paya, I. Esat, and M. Badi, "Artificial neural network based fault diagnostics of rotating machinery using wavelet transforms as a preprocessor," Mechanical Systems and Signal Processing **11**, 751–765 (1997).

[2] Z. He, W. Li, H. Salehi, H. Zhang, H. Zhou, and P. Jiao, "Integrated structural health monitoring in bridge engineering," Automation in Construction **136**, 104168 (2022).

[3] G. Song, H. Gu, Y. L. Mo, T. T. C. Hsu, and H. Dhonde, "Concrete structural health monitoring using embedded piezoceramic transducers," Smart Materials and Structures **16**, 959 (2007).

[4] T. Monnier, "Lamb waves-based impact damage monitoring of a stiffened aircraft panel using piezoelectric transducers," Journal of Intelligent Material Systems and Structures **17**, 411–421 (2006).

[5] S. Bhalla and C. K. Soh, "Structural health monitoring by piezo–impedance transducers. ii: Applications," Journal of Aerospace Engineering **17**, 166–175 (2004).

[6] C. R. "Farrar and K. Worden, *"Structural Health Monitoring"* ("John Wiley & Sons", 2013).

[7] P. Cawley and D. Alleyne, "The use of lamb waves for the long range inspection of large structures," Ultrasonics **34**, 287–290 (1996), proceedings of Ultrasonics International 1995.

[8] V. Giurgiutiu, "Tuned lamb wave excitation and detection with piezoelectric wafer active sensors for structural health monitoring," Journal of Intelligent Material Systems and Structures **16**, 291–305 (2005).

[9] W. Ostachowicz, P. Kudela, P. Malinowski, and T. Wandowski, "Damage localisation in plate-like structures based on pzt sensors," Mechanical Systems and Signal Processing **23**, 1805–1829 (2009), special Issue: Inverse Problems.

[10] V. Giurgiutiu, "Structural damage detection with piezoelectric wafer active sensors," Journal of Physics: Conference Series **305**, 012123 (2011).

[11] R. P. Palanisamy, D.-K. Pyun, and A. T. Findikoglu, "Multi-level structural damage characterization using sparse acoustic sensor networks and knowledge transferred deep learning," Ultrasonics **142**, 107390 (2024).

[12] J. Melville, K. S. Alguri, C. Deemer, and J. B. Harley, "Structural damage detection using deep learning of ultrasonic guided waves," AIP Conference Proceedings **1949**, 230004 (2018).

[13] R. Zhao, R. Yan, Z. Chen, K. Mao, P. Wang, and R. X. Gao, "Deep learning and its applications to machine health monitoring," Mechanical Systems and Signal Processing **115**, 213–237 (2019).

[14] A. Malekloo, E. Ozer, M. AlHamaydeh, and M. Girolami, "Machine learning and structural health monitoring overview with emerging technology and high-dimensional data source highlights," Structural Health Monitoring **21**, 1906–1955 (2022).

[15] J. Moll, J. Kathol, C.-P. Fritzen, M. Moix-Bonet, M. Rennoch, M. Koerdt, A. S. Herrmann, M. G. Sause, and M. Bach, "Open guided waves: online platform for ultrasonic guided wave measurements," Structural Health Monitoring **18**, 1903–1914 (2019).

[16] M. Azimi, A. D. Eslamlou, and G. Pekcan, "Data-driven structural health monitoring and damage detection through deep learning: State-of-the-art review," Sensors **20** (2020).

[17] E. Zhang, M. Dao, G. E. Karniadakis, and S. Suresh, "Analyses of internal structures and defects in materials using physics-informed neural networks," Science Advances **8**, eabk0644 (2022).

[18] B. Zhang, X. Hong, and Y. Liu, "Deep convolutional neural network probability imaging for plate structural health monitoring using guided waves," IEEE Transactions on Instrumentation and Measurement **70**, 1–10 (2021).

[19] Z. Wang, T. Han, S. Wang, Z. Zhan, W. Zhao, and S. Huang, "Health monitoring of plate structures based on tomography with combination of guided wave transmission and reflection," IEEE Sensors Journal **22**, 10850–10860 (2022).

[20] M. Lemistre and D. Balageas, "Structural health monitoring system based on diffracted lamb wave analysis by multiresolution processing," Smart Materials and Structures **10**, 504 (2001).

[21] R. Cui, G. Azuara, F. L. di Scalea, and E. Barrera, "Damage imaging in skin-stringer composite aircraft panel by ultrasonic-guided waves using deep learning with convolutional neural network," Structural Health Monitoring **21**, 1123–1138 (2022).

[22] M. Mitra and S. Gopalakrishnan, "Guided wave based structural health monitoring: A review," Smart Materials and Structures **25**, 053001 (2016).

[23] R. J. Barthorpe, *On Model- and Data-based Approaches to Structural Health Monitoring*, Phd thesis, University of Sheffield (2010), available at https://etheses.whiterose.ac.uk/1175/.

[24] S. W. Doebling, C. R. Farrar, M. B. Prime, and D. W. Shevitz, "Damage identification and health monitoring of structural and mechanical systems from changes in their vibration characteristics: A literature review," (1996).

[25] Y. Yu, C. Wang, X. Gu, and J. Li, "A novel deep learning-based method for damage identification of smart building structures," Structural Health Monitoring **18**, 143–163 (2019).

[26] T. Guo, L. Wu, C. Wang, and Z. Xu, "Damage detection in a novel deep-learning framework: a robust method for feature extraction," Structural Health Monitoring **19**, 424–442 (2020).

[27] A. Rai and M. Mitra, "Lamb wave based damage detection in metallic plates using multi-headed 1- dimensional convolutional neural network," Smart Materials and Structures **30**, 035010 (2021).

[28] H. Xu, L. Liu, J. Xu, Y. Xiang, and F.-Z. Xuan, "Deep learning enables nonlinear lamb waves for precise location of fatigue crack," Structural Health Monitoring **23**, 77–93 (2024).

[29] H. Liu and Y. Zhang, "Deep learning based crack damage detection technique for thin plate structures using guided lamb wave signals," Smart Materials and Structures **29**, 015032 (2019).

[30] A. Khan, D.-K. Ko, S. C. Lim, and H. S. Kim, "Structural vibration-based classification and prediction of delamination in smart composite laminates using deep learning neural network," Composites Part B: Engineering **161**, 586–594 (2019).

[31] M. Rautela and S. Gopalakrishnan, "Ultrasonic guided wave based structural damage detection and localization using model assisted convolutional and recurrent neural networks," Expert Systems with Applications **167**, 114189 (2021).

[32] S. Mariani, Q. Rendu, M. Urbani, and C. Sbarufatti, "Causal dilated convolutional neural networks for automatic inspection of ultrasonic signals in non-destructive evaluation and structural health monitoring," Mechanical Systems and Signal Processing **157**, 107748 (2021).

[33] D.-K. Pyun, R. P. Palanisamy, and A. T. Findikoglu, "Large-area inspection of defects in metal plates using multi-mode guided acoustic waves and sparse sensor networks," Ultrasonics **141**, 107322 (2024).

[34] P. Cawley, "Structural health monitoring: Closing the gap between research and industrial deployment," Structural Health Monitoring **17**, 1225–1244 (2018).

[35] R. Song, L. Sun, Y. Gao, C. Peng, X. Wu, S. Lv, J. Wei, and M. Jiang, "Global-local feature cross-fusion network for ultrasonic guided wave-based damage localization in composite structures," Sensors and Actuators A: Physical **362**, 114659 (2023).

[36] C. Su, M. Jiang, S. Lv, S. Lu, L. Zhang, F. Zhang, and Q. Sui, "Improved damage localization and quantification of cfrp using lamb waves and convolution neural network," IEEE Sensors Journal **19**, 5784–5791 (2019).

[37] N. P. Yelve and I. B. Mulla, "Locating damage in thin metallic plates using lamb waves and artificial neural network," in *2017 International Conference on Nascent Technologies in Engineering (ICNTE)* (2017) pp. 1–7.

[38] T. S. Cohen and M. Welling, "Group equivariant convolutional networks," (2016), arXiv:1602.07576 [cs.LG].

[39] L. Zhou, S.-X. Chen, Y.-Q. Ni, and L. Jiang, "Pitch-catch ugw-based multiple damage inference: a heterogeneous graph interpretation," Smart Materials and Structures **31**, 015005 (2021).

[40] R. Wang, R. Walters, and R. Yu, "Approximately equivariant networks for imperfectly symmetric dynamics," (2022), arXiv:2201.11969 [cs.LG].

[41] W. Shao, H. Sun, Y. Wang, and X. Qing, "A multi-level damage classification technique of aircraft plate structures using lamb wave-based deep transfer learning network," Smart Materials and Structures **31**, 075019 (2022).

[42] A. Pal, "Lux: Explicit Parameterization of Deep Neural Networks in Julia," (2023).

[43] S. Danisch and J. Krumbiegel, "Makie.jl: Flexible high-performance data visualization for Julia," Journal of Open Source Software **6**, 3349 (2021).

[44] M. Rautela, J. Senthilnath, J. Moll, and S. Gopalakrishnan, "Combined two-level damage identification strategy using ultrasonic guided waves and physical knowledge assisted machine learning," Ultrasonics **115**, 106451 (2021).

[45] D. P. Kingma and J. Ba, "Adam: A method for stochastic optimization," (2017), arXiv:1412.6980 [cs.LG].

[46] L. N. Smith and N. Topin, "Super-convergence: Very fast training of neural networks using large learning rates," (2018), arXiv:1708.07120 [cs.LG].

[47] V. Nerlikar, O. Mesnil, R. Miorelli, and O. D'Almeida, "Damage detection with ultrasonic guided waves using machine learning and aggregated baselines," Structural Health Monitoring **23**, 443–462 (2024).

[48] N. V. Chawla, K. W. Bowyer, L. O. Hall, and W. P. Kegelmeyer, "Smote: Synthetic minority over-sampling technique," Journal of Artificial Intelligence Research **16**, 321–357 (2002).

[49] J. L. Ba, J. R. Kiros, and G. E. Hinton, "Layer normalization," (2016), arXiv:1607.06450 [stat.ML].

[50]P. Ramachandran, B. Zoph, and Q. V. Le, "Searching for activation functions," (2017), arXiv:1710.05941 [cs.NE].

[51]R. Wang, R. Walters, and R. Yu, "Incorporating symmetry into deep dynamics models for improved generalization," (2021), arXiv:2002.03061 [cs.LG].

[52]M. M. Bronstein, J. Bruna, T. Cohen, and P. Veličković, "Geometric deep learning: Grids, groups, graphs, geodesics, and gauges," (2021), arXiv:2104.13478 [cs.LG].

[53]Haris Iqbal, "Harisiqbal88/plotneuralnet v1.0.0," .